

See discussions, stats, and author profiles for this publication at: <https://www.researchgate.net/publication/50865128>

# O — + Acetaldehyde Reaction Products: Search for Singlet Formylmethylene, a Wolff Rearrangement Intermediate

ARTICLE *in* THE JOURNAL OF PHYSICAL CHEMISTRY A · MARCH 2011

Impact Factor: 2.69 · DOI: 10.1021/jp112331y · Source: PubMed

---

CITATIONS

6

---

READS

35

3 AUTHORS, INCLUDING:



**Dmitry Khuseynov**

The University of Arizona

16 PUBLICATIONS 76 CITATIONS

SEE PROFILE



**Andrei Sanov**

The University of Arizona

103 PUBLICATIONS 1,450 CITATIONS

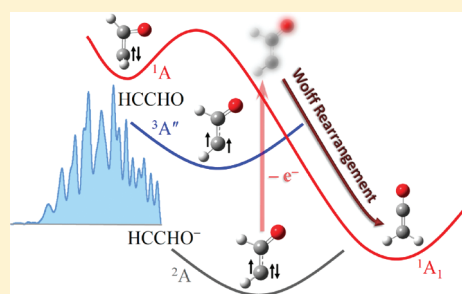
SEE PROFILE

# $O^{\bullet-}$ + Acetaldehyde Reaction Products: Search for Singlet Formylmethylene, a Wolff Rearrangement Intermediate

Daniel J. Goebbert,<sup>†</sup> Dmitry Khuseynov, and Andrei Sanov\*

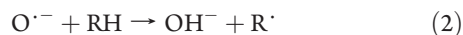
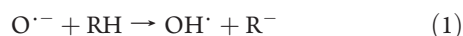
Department of Chemistry and Biochemistry, University of Arizona, Tucson, Arizona 85721, United States

**ABSTRACT:** The mass-resolved anionic products of the reaction of  $O^{\bullet-}$  with acetaldehyde,  $H_3CCHO$ , are studied using photoelectron imaging. The primary anionic products are vinoxide,  $H_2CCHO^{\bullet-}$ , formylmethylene anion,  $HCCHO^{\bullet-}$ , and ketenylidene anion,  $CCO^{\bullet-}$ . From photoelectron spectra of  $HCCHO^{\bullet-}$ , the electron affinity of triplet (ground state) formylmethylene ( $1.87 \pm 0.02$  eV) and the vertical detachment energy corresponding to the first excited triplet state (3.05 eV) are determined, but no unambiguous assignment for singlet  $HCCHO$  could be made. The elusive singlet is a key intermediate in the Wolff rearrangement, resulting in formation of ketene. The fast rearrangement associated with a large geometry change upon photodetachment to the singlet surface may be responsible for the low intensity of the singlet compared to the triplet bands in the photoelectron spectrum. The title reaction also yields  $CCO^{\bullet-}$ , whose formation from acetaldehyde is novel and intriguing, since it requires a multistep net- $H_4^+$  abstraction. A possible mechanism is proposed, involving an  $[H_2CCO^{\bullet-}]^*$  intermediate. From the measured electron affinities of  $HCCHO$  (above),  $H_2CCHO$  ( $1.82 \pm 0.01$  eV), and  $CCO$  ( $2.31 \pm 0.01$  eV), several new thermochemical properties are determined, including the C–H bond dissociation energies and heats of formation of several organic molecules and/or their anions. Overall, the reactivity of  $O^{\bullet-}$  with organic molecules demonstrates the utility of this anion in the formation of a variety of reactive intermediates via a single process.



## 1. INTRODUCTION

The gas-phase reactivity of atomic oxygen radical anion ( $O^{\bullet-}$ ) with organic molecules is well documented.<sup>1–5</sup> This anion primarily reacts with organics via  $H^+$ ,  $H^{\bullet}$ , or  $H_2^{*+}$  abstraction, as indicated by the respective reactions:



These reactions are extremely useful, as they provide a convenient method for gas-phase synthesis of a number of important anion intermediates. These intermediates can be characterized by spectroscopy, reactivity, or fragmentation in order to obtain their thermochemical properties, as well as molecular and electronic structures. However, one disadvantage of  $O^{\bullet-}$  as a reagent is that it is often unselective toward the site of deprotonation, resulting in a complex mixture of isomers. Thus,  $O^{\bullet-}$  is most useful as a reagent when a limited number of H atoms are available.

The reaction of  $O^{\bullet-}$  with acetaldehyde,  $H_3CCHO$ , was examined previously by Grabowski and Melly using the flowing afterglow technique.<sup>5</sup> The products observed were  $H_2CCHO^{\bullet-}$  (34%),  $HCCHO^{\bullet-}$  (32%),  $OH^{\bullet-}$  (9%),  $H_3CCO_2^{\bullet-}$  (15%), and  $HCO_2^{\bullet-}$  (10%). The primary products correspond to the reactions 1–3, while the minor products result from the addition of  $O^{\bullet-}$ , followed by elimination.

Of the above products, particularly interesting is the formylmethylene anion,  $HCCHO^{\bullet-}$ . Electron detachment from this anion yields formylmethylene, an important carbene intermediate in the Wolff rearrangement.<sup>6,7</sup> This reaction is widely used in chemistry, especially in the synthesis of acids, ring contractions, and most importantly in the industrial process of photolithography.<sup>6</sup> Although formylmethylene could be found in several low energy electronic states (triplet and singlet), it is the singlet that is involved in the Wolff rearrangement.

The general mechanism of the Wolff rearrangement via a formylmethylene intermediate is shown in Figure 1. Typically,  $HCCHO$ , **1**, is generated by pyrolysis or photolysis of a diazoketone. The carbene undergoes a 1,2-H atom shift to form ketene,  $H_2CCO$ , **3**. Isotopic labeling studies have shown the carbon atoms in  $H_2CCO$  scramble, so an oxirene intermediate, **2**, has been proposed to explain experimental observations.

Although Figure 1 provides a plausible mechanism for the Wolff rearrangement, several experiments have indicated the reaction is controlled by additional factors, such as precursor geometry.<sup>6–8</sup> For example, photolysis of *syn*- $\alpha$ -diazoketones leads preferentially to the formation of ketenes, while photolysis of *anti*- $\alpha$ -diazoketones, such as 2,2,5,5-tetramethyl-4-diazo-3-hexanone does not always lead to significant yields of ketene products.<sup>8</sup> Time-resolved studies have indicated there are at least

Received: December 28, 2010

Revised: March 2, 2011

Published: March 25, 2011

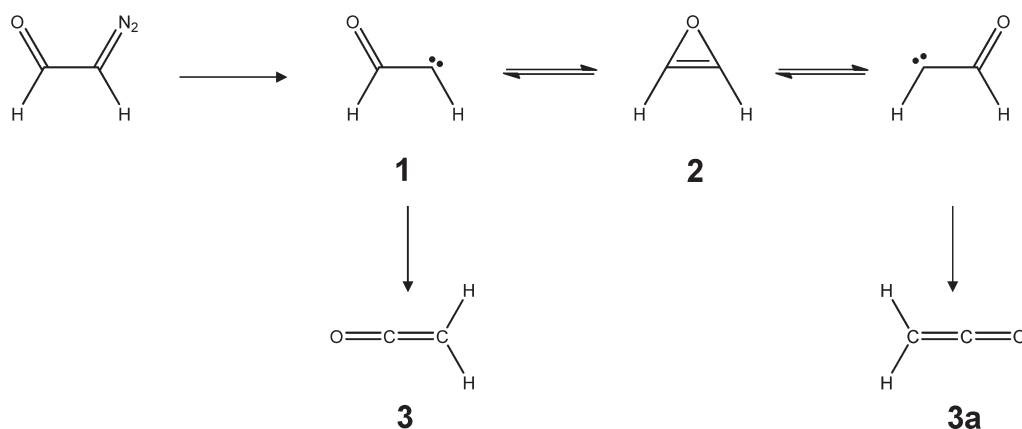


**Figure 1.** General mechanism for the Wolff rearrangement of formylmethylene, **1**, to ketene, **3**, via the oxirene intermediate, **2**, allowing carbon atom scrambling.

two decay processes related to the starting geometry of the ketocarbene intermediate.<sup>9,10</sup> A fast decay is consistent with a direct 1,2-H atom shift immediately upon photolysis. A slower component would imply the formation of a long-lived intermediate, such as oxirene or a ketocarbene. A recent study found evidence for nonstatistical behavior in the product ratio of the Wolff rearrangement due to a bifurcated potential energy surface.<sup>11</sup> Thus, the mechanism in Figure 1 is too general for this reaction.

In this paper, we report a photoelectron imaging study of the products from the reaction of  $\text{O}^{\bullet-}$  with acetaldehyde. The primary purpose of the study was to investigate  $\text{HCCHO}$  via electron detachment of the formylmethylene anion. This approach provides an alternate pathway to generation of  $\text{HCCHO}$ , unlike the traditional decomposition of diazoketones. In addition, we investigate several other reactive intermediates formed in the  $\text{O}^{\bullet-} + \text{H}_3\text{CCHO}$  reaction, including vinoxide,  $\text{H}_2\text{CCHO}^-$ , and an apparent two-step reaction product,  $\text{CCO}^{\bullet-}$ . Both intermediates are characterized in comparison with previously recorded photoelectron spectra reported in refs 12–14 and refs 15 and 16, respectively.

## 2. EXPERIMENTAL AND THEORETICAL METHODS

The experiments were carried out using a pulsed negative-ion time-of-flight photoelectron imaging spectrometer described previously.<sup>17</sup> A mixture of room-temperature acetaldehyde vapor in  $\text{N}_2\text{O}$  carrier gas at a pressure of 30 psi was expanded into a vacuum chamber using a General Valve (series 99) pulsed supersonic nozzle. Anions were generated by collisions of 1 keV electrons from an electron gun, creating slow secondary electrons. The slow electrons undergo dissociative attachment to  $\text{N}_2\text{O}$  to form  $\text{O}^{\bullet-}$ . The nascent  $\text{O}^{\bullet-}$  reacts further via chemical ionization, as in eqs 1 – 3.

The anions were mass selected in a linear time-of-flight mass spectrometer and intersected by a pulsed linearly polarized laser beam (Nd:YAG, 10 ns, 30 mJ at 532 nm or 10 mJ at 355 nm) within a velocity-map<sup>18</sup> imaging<sup>19</sup> assembly. Photodetached electrons were projected onto a microchannel-plate detector, coupled to a phosphor screen. The resulting images were recorded by a charge-coupled device camera. The images were accumulated for statistics and analyzed by inverse Abel transformation using the BASEX program.<sup>20</sup> Transformed images yield intensities in radial and angular coordinates with respect to the

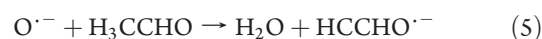
image center,  $I(r, \theta)$ , where angle  $\theta$  is defined relative to the laser polarization direction. Photoelectron spectra are obtained by integrating the transformed images with respect to the angular coordinate. The spectra were calibrated using the known photoelectron spectrum of  $\text{O}^{\bullet-}$ .<sup>21,22</sup> Photoelectron angular distributions (PADs) were obtained by integration over  $r$ . The angular distributions were fit using the standard equation<sup>23</sup> and characterized in terms of the anisotropy parameter  $\beta$ .<sup>24,25</sup>

Electronic structure calculations were carried out using the Gaussian 03 program.<sup>26</sup> Unless stated otherwise, the geometry optimizations and frequency calculations reported in this work were performed at the B3LYP/aug-cc-pVDZ level of theory. Other basis sets, aug-cc-pVQZ and 6-311++G(3df,3pd), were also used, for comparison, but only small differences were found. For the  $\text{HCCHO}^{\bullet-}$  and  $\text{HCCHO}$ , we also employed the Møller–Plesset second-order perturbation theory (MP2), in order to compare the predictions of different methods. Frequency calculations were used to confirm that the optimized structures corresponded to local minima. Transition state structures were identified as structures with a single imaginary frequency.

## 3. EXPERIMENTAL RESULTS AND ANALYSIS

A representative mass spectrum of the ions formed by the reaction of  $\text{O}^{\bullet-}$  with  $\text{H}_3\text{CCHO}$  seeded in  $\text{N}_2\text{O}$  is shown in Figure 2. The  $\text{O}^{\bullet-} + \text{H}_3\text{CCHO}$  reaction products are indicated with red arrows and labels. Similar to the high-pressure flow-tube results,<sup>2</sup> we observe the vinoxide anion,  $\text{H}_2\text{CCHO}^-$  ( $m/z = 43$  amu) and the formylmethylene anion,  $\text{HCCHO}^{\bullet-}$  ( $m/z = 42$  amu). In addition, we observe an  $m/z = 40$  amu peak assigned to the ketenylidene anion,  $\text{CCO}^{\bullet-}$ . The peaks marked with asterisks are possible addition/elimination products,  $\text{HCO}_2^-$  and  $\text{H}_3\text{CCO}_2^-$ , similar to those observed in the high-pressure flow-tube reactor.<sup>2</sup> However, these ions could not be investigated spectroscopically, because of their low intensities and large electron affinities.

The primary products of the reaction of  $\text{O}^{\bullet-}$  with  $\text{H}_3\text{CCHO}$  are formed via the following pathways:



Formation of  $\text{CCO}^{\bullet-}$  requires removal of all four H centers (three H atoms and a proton,  $\text{H}^+$ ) in  $\text{H}_3\text{CCHO}$ . Such elimination

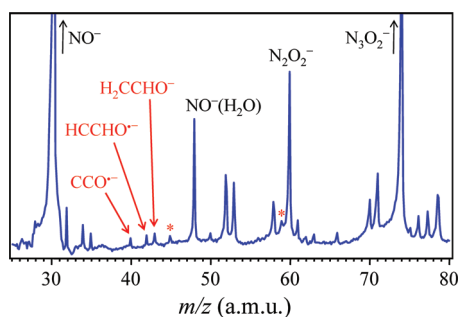


**Figure 2.** Time-of-flight mass spectrum of the negative ions formed in the reaction of  $\text{O}^{\bullet-}$  with  $\text{H}_3\text{CCHO}$  seeded in  $\text{N}_2\text{O}$  carrier gas at a backing pressure of 30 psi. The vertical scale is magnified to emphasize the low-intensity peaks. The major peaks (black labels) correspond to  $\text{N}_x\text{O}_y^-$  species resulting from the reaction of  $\text{O}^{\bullet-}$  with  $\text{N}_2\text{O}$ . The  $\text{O}^{\bullet-} + \text{H}_3\text{CCHO}$  reaction products,  $\text{CCO}^-$  ( $m/z = 40$ ),  $\text{HCCHO}^-$  ( $m/z = 42$ ), and  $\text{H}_2\text{CCHO}^-$  ( $m/z = 43$ ) are indicated with red arrows and corresponding labels. The peaks marked with red asterisks could correspond to the addition/elimination products  $\text{HCO}_2^-$  ( $m/z = 45$ ) and  $\text{CH}_3\text{CO}_2^-$  ( $m/z = 59$ ); however, because of low ion intensity, we could not obtain photoelectron spectra of these ions to confirm the assignment.

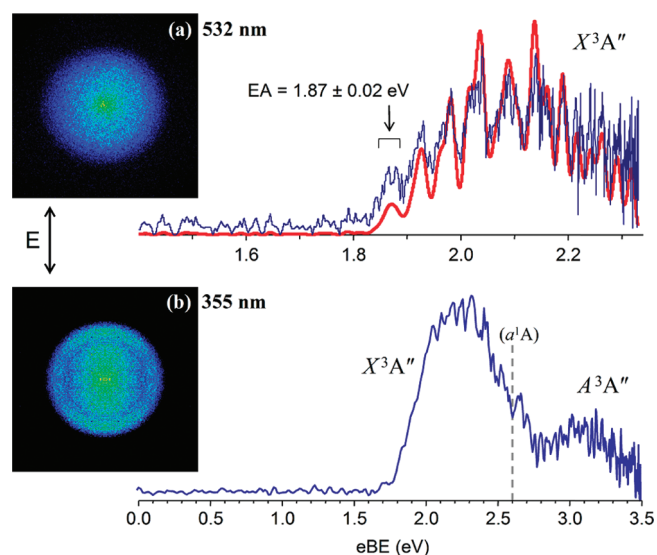


**Figure 3.** Photoelectron images and spectra of formylmethylene anion,  $\text{HCCHO}^{\bullet-}$ , measured at 532 and 355 nm. In a, the 532 nm experimental spectrum (blue) corresponding to the ground  $X^3A''$  state of  $\text{HCCHO}$ , is superimposed with the filtered spectrum (red), obtained using a low-pass Fourier filter, as described in the text. In b, the 355 nm image and spectrum show two bands corresponding to the  $X^3A''$  and  $A^3A''$  states of  $\text{HCCHO}$ . The vertical dashed line indicates the approximate location of the  $a^1A$  state, expected based on the calculations described in the text.

must be at least a two-step process, and a possible mechanism is proposed in section 4.2.

The product anions were characterized individually by photoelectron imaging. The  $\text{HCCHO}^{\bullet-}$  anion had not been previously studied by photoelectron spectroscopy, and we carried out both spectroscopic and theoretical investigations of  $\text{HCCHO}^{\bullet-}$  and  $\text{HCCHO}$  in the ground and excited states. The experimental results for this ion are presented in section 3.1 and discussed in detail in section 4.1. The  $\text{H}_2\text{CCHO}^-$  and  $\text{CCO}^{\bullet-}$  ions, on the

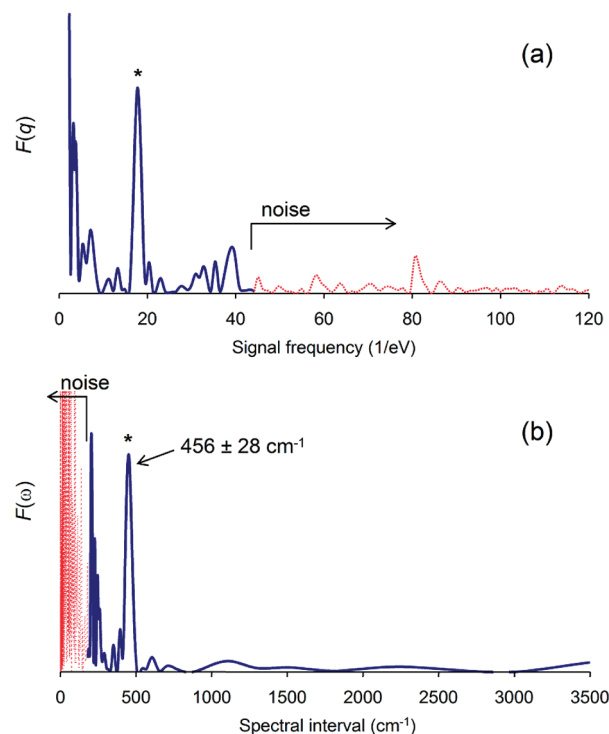


**Figure 4.** (a) Fourier transform  $F(q)$  of the experimental 532 nm photoelectron spectrum of  $\text{HCCHO}^{\bullet-}$  in Figure 3a. The Fourier spectrum is arbitrarily divided into the low- $q$  (true signal) and high- $q$  (noise) parts, shown as a solid blue and red dotted lines, respectively. The high- $q$  (noise) part is discarded in calculating the filtered spectrum shown in Figure 3a. (b) The same Fourier spectrum as in a, but plotted as a function of periodic spectral interval  $\omega$ , related to signal frequency  $q$  by  $\hbar\omega = 1/q$ .  $F(\omega)$  is obtained from  $F(q)$  via a Jacobian transformation  $F(\omega) = F(q) |dq/d\omega|$ , with  $|dq/d\omega| \propto q^2$ . The blue solid and red dotted lines have the same meaning as in a. Asterisks mark the same dominant vibrational peak at  $q = 17.7 \text{ eV}^{-1}$  in a, corresponding to  $\omega = 456 \text{ cm}^{-1}$  in b, reflecting the average spacing of the partially resolved vibrational progression seen in the experimental spectrum in Figure 3a.

other hand, have been the targets of several previous experiments,<sup>12–16,27,28</sup> and only brief discussions of their photoelectron spectra are included in sections 3.2 and 3.3, respectively. These analyses are necessary not only for completeness of the present study but also because the resulting energetics are used in determining several thermochemical properties in section 4.3.

**3.1. Formylmethylene Anion,  $\text{HCCHO}^-$ .** The 532 and 355 nm photoelectron images and spectra of formylmethylene anion,  $\text{HCCHO}^-$  ( $m/z = 42$  in Figure 2), are shown in Figure 3. The 532 nm image (a) shows a single feature assigned to the  $X^3A''$  ground state of  $\text{HCCHO}$ . To analyze the partially resolved vibrational structure, we performed a Fourier transform of the spectrum:  $f(\text{eBE}) \rightarrow F(q)$ , where  $q$  is signal frequency (in units of  $1/\text{eV}$ ), conjugate to electron binding energy (eBE). The result,  $F(q)$ , is plotted in Figure 4a. The high- $q$  part of the Fourier spectrum (red dotted line) corresponds to noise in the experimental data, while other dominant features of  $F(q)$  (blue solid line) reflect the periodic components present in the original spectrum in Figure 3a. In particular, the peak at  $q = 17.7 \text{ eV}^{-1}$ , marked in Figure 4a with an asterisk, corresponds to the dominant vibrational progression discerned in the photoelectron spectrum in Figure 3a. The features near  $q = 0$  in Figure 4a define the overall envelope of the  $X^3A''$  spectral band in Figure 3a.



Figure 4b shows the same Fourier spectrum, but plotted as a function of  $\omega$ , defined as the periodic spectral interval corresponding to signal frequency  $q$ :  $\hbar\omega = 1/q$ .  $F(\omega)$  is obtained from  $F(q)$  via a Jacobian transformation:  $F(\omega) = F(q) |dq/d\omega|$ , where  $|dq/d\omega| \propto q^2$ .  $F(\omega)$  is the spectrum of (vibrational) mode frequencies present in the experimental spectrum  $f(\text{eBE})$ . The high- $q$  (noise) part of the Fourier spectrum in Figure 4a corresponds to the low- $\omega$  part of  $F(\omega)$ , while the dominant vibrational peak at  $q = 17.7 \text{ eV}^{-1}$  transforms into the corresponding peak, also marked with an asterisk, in Figure 4b. From the maximum position and width of this peak, we determine the average spacing of the partially resolved vibrational progression in Figure 3a as  $456 \pm 28 \text{ cm}^{-1}$ .

We further used the Fourier analysis as a low-pass filter for the 532 nm experimental spectrum shown in Figure 3a. Specifically, the high- $q$  (low- $\omega$ ) noise part of the Fourier spectrum was eliminated (replaced by zeros) and the resulting cleaned up spectrum, consisting only of the blue solid part in Figure 4, was used for inverse Fourier transform. This procedure yielded the filtered photoelectron spectrum shown as a solid red line in Figure 3a. The vibrational progression with the average spacing determined above is unmistakable in the filtered spectrum. Assigning the first peak of the filtered  $X^3A''$  spectral band as the band origin yields the adiabatic electron affinity of  $\text{HCCHO}$ ,  $\text{EA} = 1.87 \pm 0.02 \text{ eV}$ .

The 355 nm image in Figure 3b shows a second spectral feature, with a maximum around 3.05 eV. This feature is assigned to an excited state of  $\text{HCCHO}$ ,  $A^2A'$ . Both bands,  $X^3A''$  and  $A^2A'$ , have maximum intensities parallel to the laser polarization, corresponding to  $\beta > 0$ .

**3.2. Vinoxide Anion,  $\text{H}_2\text{CCHO}^-$ .** The vinoxide anion,  $\text{H}_2\text{CCHO}^-$ , has been the subject of several previous studies.<sup>29–32</sup> Most recently, a high-resolution slow-electron velocity-map imaging (SEVI) study gave an adiabatic electron affinity  $\text{EA}(\text{H}_2\text{CCHO}^*) = 1.8250 \pm 0.0012 \text{ eV}$ .<sup>12</sup> This result is compared to the EA values of  $1.8248 \text{ eV}$ ,<sup>31</sup>  $1.817 \pm 0.023 \text{ eV}$ ,<sup>29</sup> and  $1.8240 \pm 0.0050 \text{ eV}$ ,<sup>32</sup> obtained in earlier studies. A photoelectron image of  $\text{H}_2\text{CCHO}^-$  has also been reported previously,<sup>13</sup> giving an  $\text{EA} = 1.795 \pm 0.015 \text{ eV}$ .<sup>14</sup> Our results for this species are consistent with the previous studies and hence only a brief account is given here.

The 355 and 532 nm photoelectron images and spectra of  $\text{H}_2\text{CCHO}^-$  (corresponding to  $m/z = 43$  in Figure 2) are shown in Figure 5. The 355 nm image shows two major features, a low energy band assigned to the  $X^2A''$  state of vinoxy and a higher energy feature assigned to the first excited state,  $A^2A'$ . The 532 nm spectrum shows a vibrational progression for the ground state only. Its onset allows for an unambiguous determination of adiabatic electron affinity,  $\text{EA}(\text{H}_2\text{CCHO}^*) = 1.82 \pm 0.01 \text{ eV}$  ( $42.0 \pm 0.2 \text{ kcal/mol}$ ), is in good agreement with the above SEVI experiment<sup>12</sup> and other previous studies.<sup>13,14,29,31,32</sup> It also agrees with the theoretical prediction of  $1.84 \text{ eV}$  [B3LYP/6-311++G(3df,3pd)]. The  $557 \pm 70 \text{ cm}^{-1}$  spacing between the partially resolved peaks in the  $X^2A''$  band (532 nm) is assigned to the CCO bending mode. Contributions from other modes (primarily due to CC and CO stretches) overlap with the main progression, resulting in additional structure and broadening of the bands in Figure 5.<sup>12,14</sup>

The first excited state of  $\text{H}_2\text{CCHO}^*$ ,  $A^2A'$ , also shows vibrational structure, with an onset at  $2.80 \pm 0.01 \text{ eV}$  and an apparent spacing of about  $1500 \text{ cm}^{-1}$ . The band origin corresponds to a  $0.98 \pm 0.02 \text{ eV}$  term energy for the  $A^2A'$  excited state of vinoxy radical, in agreement with the SEVI result of  $0.996 \pm 0.003 \text{ eV}$ .<sup>12</sup>

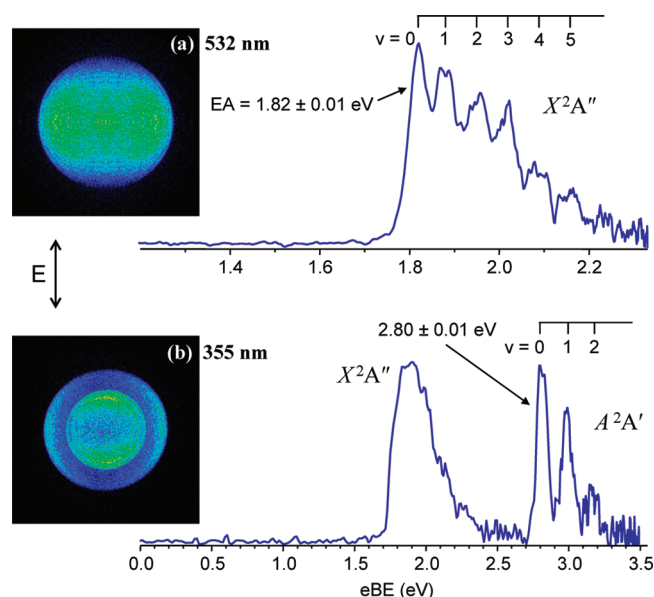


**Figure 5.** Photoelectron images and spectra of vinoxide,  $\text{H}_2\text{CCHO}^-$ , measured at (a) 532 and (b) 355 nm. The 532 nm spectrum shows the ground  $X^2A''$  state and a vibrational progression with the peaks labeled  $v = 0-5$ . The 355 nm spectrum also shows the  $X^2A''$  state and the excited  $A^2A'$  state with a vibrational progression labeled  $v = 0-2$ .

The  $\sim 1500 \text{ cm}^{-1}$  vibrational progression for the  $A^2A'$  state at 355 nm (Figure 5) is in good agreement with the  $1595 \text{ cm}^{-1}$  (unscaled) frequency of the CC stretch calculated at the B3LYP/6-311++G(3df,3pd) level. Several other modes, primarily the CO stretch, also contribute to the overall band shape.<sup>12,14</sup>

The  $X^2A''$  transition exhibits perpendicular angular distributions at both wavelengths studied, corresponding to  $\beta = -0.64(5)$  at 355 nm. The excited state has a parallel distribution, with  $\beta = 0.51(5)$  determined for the first two vibrational features in the 355 nm image. Continetti and co-workers<sup>13</sup> interpreted the photoelectron angular distributions in  $\text{H}_2\text{CCHO}^-$  photodetachment using symmetry-based arguments.<sup>33</sup> In the dominant electron configuration of  $\text{H}_2\text{CCHO}^-$ ,  $[\text{core}](10a')^2(2a'')^2$ , the  $2a''$  HOMO is a nonbonding  $\pi$  orbital, while the  $10a'$  HOMO-1 is essentially an oxygen lone-pair with significant "s" character in the plane of the molecule. Electron detachment from the  $10a'$  orbital is expected to yield a predominantly parallel angular distribution, while detachment from  $2a''$  should yield a perpendicular distribution. Thus, the perpendicular and parallel features seen in Figure 5 are consistent with the formation of  $\text{H}_2\text{CCHO}$  in the  $X^2A''$  and  $A^2A'$  states, respectively.

**3.3. Ketenylidene Anion,  $\text{CCO}^{*-}$ .** The 355 nm photoelectron image and photoelectron spectrum of  $\text{CCO}^{*-}$  ( $m/z = 40$  in Figure 2) are shown in Figure 6. The results are in excellent agreement with previous findings for  $\text{CCO}^{*-}$  (not involving the title reaction),<sup>15,16,27</sup> leaving no doubt about the identity of the observed species. All image features peak in the direction perpendicular to the laser polarization, corresponding to negative  $\beta$  values, as expected for electron emission from a d-like  $\pi^*$  HOMO of  $\text{CCO}^{*-}$ .

The spectrum shows a number of well-resolved vibrational peaks. The first set of peaks is assigned to the ground state of  $\text{CCO}$ ,  $X^3\Sigma^-$ , and the origin yields  $\text{EA} = 2.31 \pm 0.01 \text{ eV}$ , in agreement with the previously reported values of  $2.3207 \pm 0.0006 \text{ eV}$  (SEVI)<sup>15</sup> and  $2.310 \pm 0.012 \text{ eV}$  (photoelectron

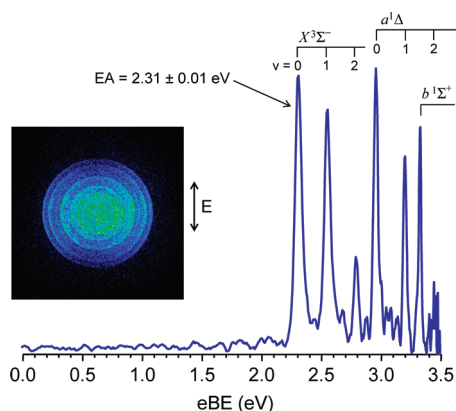


**Figure 6.** Photoelectron image and spectrum of  $\text{CCO}^{*-}$  obtained at 355 nm. The  $X^3\Sigma^-$ ,  $a^1\Delta$ , and  $b^1\Sigma^+$  electronic states are observed, with the well-resolved vibrational progressions corresponding to the C=O stretch. Lower intensity peaks are due to the C=C stretch mode.

spectroscopy).<sup>28</sup> The higher-energy peaks are assigned to the first,  $a^1\Delta$ , and second,  $b^1\Sigma^+$ , excited states of  $\text{CCO}$ . The sharp origin transitions are used to assign the adiabatic detachment energies:  $2.95 \pm 0.01$  eV for the  $a^1\Delta$  state and  $3.33 \pm 0.01$  eV for  $b^1\Sigma^+$ . The corresponding term energies are  $0.64 \pm 0.01$  and  $1.02 \pm 0.01$  eV, respectively, compared to the SEVI values  $0.6539 \pm 0.0006$  and  $1.0170 \pm 0.0006$  eV.<sup>15</sup> The major progressions comprising the  $X^3\Sigma^-$  and  $a^1\Delta$  bands, spaced by about  $1970\text{ cm}^{-1}$  in both cases, are assigned to CO stretch.

#### 4. DISCUSSION

The major products formed from the reaction of  $\text{O}^{*-}$  with  $\text{H}_3\text{CCHO}$  are  $\text{CCO}^{*-}$ ,  $\text{HCCHO}^{*-}$ , and  $\text{H}_2\text{CCHO}^-$ . Of these,  $\text{HCCHO}^{*-}$  and  $\text{H}_2\text{CCHO}^-$  were observed previously,<sup>5</sup> but  $\text{CCO}^{*-}$  was not. Although  $\text{HCCHO}^{*-}$  was previously detected in the above reaction, it has not been studied by photoelectron spectroscopy. In section 4.1, we discuss our findings for  $\text{HCCHO}^{*-}$  and the corresponding neutral molecule. In section 4.2, a mechanism of  $\text{CCO}^{*-}$  formation is proposed. Section 4.3 summarizes the thermochemical properties derived from our measurements.

**4.1. Formylmethylene: Anion and Neutral Structures and the Wolff Rearrangement.** The formation of  $\text{HCCHO}^{*-}$  in the  $\text{O}^{*-} + \text{H}_3\text{CCHO}$  reaction was reported by Grabowski and Melly.<sup>5</sup> The photodetachment of this anion gives formylmethylene, an intermediate in the Wolff rearrangement (see Figure 1).

The electronic structures of three lowest-energy electronic states of  $\text{HCCHO}$ , the ground-state triplet ( $^3\text{HCCHO}$ ), the singlet ( $^1\text{HCCHO}$ ), and the excited-state triplet, are illustrated in Figure 7 for a planar molecular geometry with the H atoms in the cis configuration. In the ground state, the carbene structure has one electron in a  $\sigma$  and one in a  $\pi$  orbital. There is also a resonance structure with the unpaired  $\pi$  electron on the oxygen atom; this structure is best described as a  $\sigma,\pi$  biradical. Qualitative predictions suggest the carbene form is the primary resonance structure, so the biradical character of  $X^3A''$  is usually ignored.

In the singlet carbene at a planar geometry (corresponding to the  $a^1A'$  state), both electrons are paired in the carbon  $\sigma$  orbital, while the corresponding resonance structure with a C=C double bond is zwitterionic (Figure 7). However, the planar geometry is not the lowest energy structure of  $^1\text{HCCHO}$ . It twists around the C—C bond, forming the lower energy nonplanar structure. The nonplanarity is an important property of singlet formylmethylene.<sup>34–36</sup>

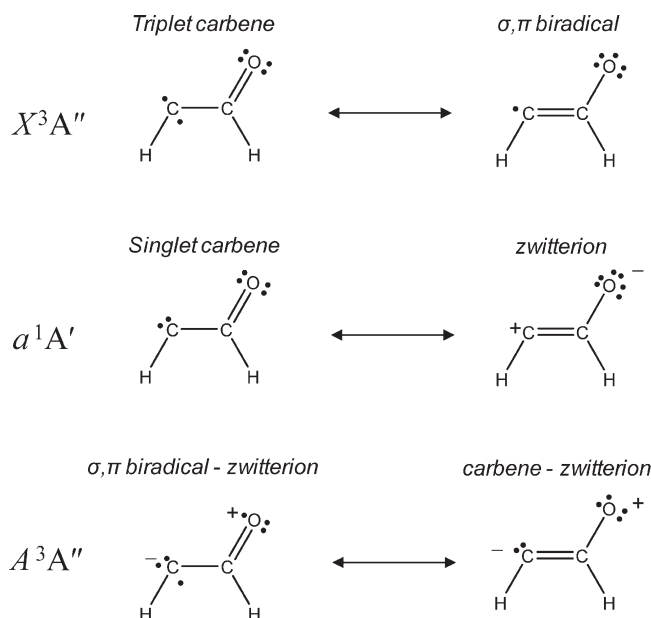


**Figure 7.** The lowest electronic states of  $\text{HCCHO}$ ,  $X^3A''$ ,  $a^1A'$ , and  $A^3A''$  in order of increasing energy. The primary resonance structures for each state are labeled to best describe the electron arrangement.

The excited triplet state,  $A^3A''$ , results from removal of an electron from the oxygen lone pair in the anion, producing a zwitterionic species best described as a  $\sigma,\pi$  biradical. In this state, there is an unpaired electron in the  $\pi$  system, which is resonance stabilized in a carbene zwitterionic structure. However, the  $\sigma,\pi$  biradical form is expected to be the primary resonance structure of the  $A^3A''$  state.

The geometries of precursors are known to play a role in determining the rearrangement products of carbonyl-carbenes.<sup>6,7</sup> In our investigation of  $\text{HCCHO}^{*-}$ , both B3LYP and MP2 methods predict the nonplanar syn geometry of  $\text{HCCHO}^{*-}$  is the global minimum, while the anti geometry equilibrium is predicted to lie about 0.05 eV (1.1 kcal/mol) higher in energy.<sup>37</sup> To guide our analysis, we performed an inexpensive, albeit admittedly crude, relaxed potential energy surface scan with respect to the H—C—C(O)—H dihedral angle at the B3LYP/aug-cc-pVDZ level of theory. The result, plotted in Figure 8, shows a 0.15 eV (3.5 kcal/mol) barrier to interconversion. The dihedral angle corresponding to the minimum-energy structure is approximately  $40^\circ$ . On the basis of these findings, we expect the syn conformation of  $\text{HCCHO}^{*-}$  to be favored.

The ground state of neutral formylmethylene is a planar-geometry triplet. A similar potential energy surface scan (Figure 8) shows that the global minimum of  $\text{HCCHO}$  corresponds to a trans geometry, with the cis structure as a local minimum about 0.04 eV (1 kcal/mol) higher in energy. The barrier to cis—trans interconversion is predicted to be 0.30 eV (7 kcal/mol). Hence, we expect vertical electron detachment from the syn global minimum of the anion (VDE = 2.22 eV at the B3LYP/aug-cc-pVDZ level of theory) to yield the higher-energy *cis*- $^3\text{HCCHO}$  isomer with a calculated adiabatic electron affinity (relative to *syn*- $\text{HCCHO}^{*-}$ ) of about 1.93 eV. Vertical detachment from the slightly higher-energy anti anion (VDE = 2.18 eV at the B3LYP/aug-cc-pVDZ level of theory) would lead to the lower-energy *trans*- $^3\text{HCCHO}$ , with a calculated adiabatic electron affinity (relative to *anti*- $\text{HCCHO}^{*-}$ ) of about 1.83 eV.

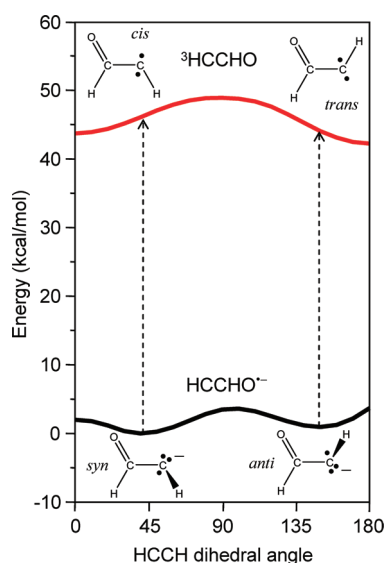


**Figure 8.** Relaxed potential energy surface scan of the HCCH dihedral angle for  $\text{HCCHO}^{*-}$  and  ${}^3\text{HCCHO}$  calculated at the B3LYP/aug-cc-pVDZ level of theory. The predicted lowest-energy structure for  $\text{HCCHO}^{*-}$  is the syn geometry, while the anti structure is about 1 kcal/mol higher in energy. The lowest energy structure of  ${}^3\text{HCCHO}$  is the trans isomer, with a barrier of about 3.5 kcal/mol separating the cis and trans isomers.

The 532 nm photoelectron spectrum of  $\text{HCCHO}^{*-}$  in Figure 3a is congested, because of the overlap of many vibrational modes of  ${}^3\text{HCCHO}$  excited upon  $\text{HCCHO}^{*-}$  photodetachment. The electron affinity of  ${}^3\text{HCCHO}$  is determined to be  $1.87 \pm 0.02$  eV, in good agreement with the calculated values for both the trans- and cis- forms of  ${}^3\text{HCCHO}$  (1.83 and 1.93 eV, respectively). The spectrum in Figure 3a does show a vibrational progression, with an average spacing of  $456 \pm 28$   $\text{cm}^{-1}$ , as determined by the Fourier analysis described in section 3.1. The major geometry difference between the anion and neutral is the H–CC(O)–H dihedral angle, and so we expect the H–CC(O)–H out-of-plane bend to be the primary vibration excited upon photodetachment. The observed spectral interval is in good agreement with the fundamental frequency of this mode in *cis*- ${}^3\text{HCCHO}$ , calculated to be 492  $\text{cm}^{-1}$  (unscaled, B3LYP/aug-cc-pVQZ level of theory). This observation suggests the predominant presence of *syn*- $\text{HCCHO}^{*-}$ , consistent with the lower energy of the syn (compared to anti) conformation, as predicted by theory.

The same mode for the *trans*- ${}^3\text{HCCHO}$  structure has a 626  $\text{cm}^{-1}$  frequency, which is intriguingly close to the location of a secondary spectral feature at  $608 \pm 30$   $\text{cm}^{-1}$  in Figure 4b, just to the right of the main (\*) peak. Although the intensity of this secondary feature is too small to draw solid conclusions, we find that the integrated intensity ratio of the two peaks ( $\sim 20:1$ ) is consistent with a statistical distribution of the *syn*- and *anti*- $\text{HCCHO}^{*-}$  isomers, given the predicted energy difference (1.1 kcal/mol) and assuming an ion-beam (vibrational) temperature of  $\sim 200$  K.

The higher-energy feature in the 355 nm photoelectron spectrum of  $\text{HCCHO}^{*-}$  in Figure 3b is attributed to the excited triplet state,  $A^3A''$ , which arises from electron detachment of an oxygen lone-pair in  $\text{HCCHO}^{*-}$  (see Figure 7) with a calculated VDE of 3.00 eV (B3LYP/aug-cc-pVDZ). This prediction compares well with the band maximum observed at about 3.05 eV.

On the basis of various theoretical predictions, the  $\text{HCCHO}^{*-} \rightarrow {}^1\text{HCCHO}$  photodetachment transition is expected at  $\text{eBE} \geq 2.60$  eV, slightly higher in energy than  ${}^3\text{HCCHO}$ , but below the excited triplet,  $A^3A''$ . The photoelectron spectrum shows no clear evidence for  ${}^1\text{HCCHO}$ . The expected location of this transition, based on B3LYP/aug-cc-pVDZ, is indicated in Figure 3b by a dashed line. Although there is spectral intensity in this region, it is impossible to conclude if it is due to  ${}^1\text{HCCHO}$  or the  $X^3A''$  band, or both.

Geometry optimization for  ${}^1\text{HCCHO}$ , starting from the global-minimum *syn* structure of  $\text{HCCHO}^{*-}$ , at all levels of theory used in this study, leads to ketene,  $\text{H}_2\text{CCO}$ . This result is in accord with previous observations that *syn*-ketocarbenes preferentially form ketene products. It also agrees with the time-resolved studies<sup>9,10,38</sup> that indicated a fast, direct rearrangement for *syn*-ketocarbenes. On the other hand, optimization of  ${}^1\text{HCCHO}$  geometry starting from the *anti*- $\text{HCCHO}^{*-}$  structure yielded a stable minimum corresponding to *anti*- ${}^1\text{HCCHO}$ , separated from ketene by a small barrier. Figure 9 summarizes the neutral product correlations for *syn*- and *anti*- $\text{HCCHO}^{*-}$  photodetachment, including the *anti*- ${}^1\text{HCCHO} \rightarrow \text{H}_2\text{CCO}$  transition state. At the B3LYP/aug-cc-pVDZ level of theory, vertical detachment of *anti*- $\text{HCCHO}^{*-}$  yields  ${}^1\text{HCCHO}$  with an energy approximately equivalent to the transition state and the resulting neutral molecule is likely to undergo a 1,2-H atom shift to ketene. Overall, detachment to the singlet state is expected to result in a fast Wolff rearrangement to  $\text{H}_2\text{CCO}$ , regardless of the starting geometry of  $\text{HCCHO}^{*-}$ . The transient nature of  ${}^1\text{HCCHO}$  contrasts that of  ${}^3\text{HCCHO}$ , which is a long-lived species, not subject to the Wolff rearrangement.

Although both  $\text{HCCHO}^{*-}$  and  ${}^1\text{HCCHO}$  are nonplanar at their respective equilibria, the geometry difference between the two is more significant than that of the anion and  ${}^3\text{HCCHO}$  (see Figure 9). Because of the large difference between the equilibrium geometries of  $\text{HCCHO}^{*-}$  and  ${}^1\text{HCCHO}$  (or  $\text{H}_2\text{CCO}$ ), we expect these transitions to have poor Franck–Condon overlap and hence low intensity, compared to  ${}^3\text{HCCHO}$ . Photoelectron (transition-state) spectroscopy, is often a powerful tool for probing short-lived intermediates. For example, this utility is clearly born out in the studies of vinylidenes<sup>39,40</sup> and oxyallyl.<sup>41–43</sup> However, to observe a short-lived intermediate, it must either be well separated in the photoelectron spectrum from other transitions or exhibit identifiable characteristic vibrational structure. In this study, the  ${}^1\text{HCCHO}$  transition is expected to have low intensity due to a poor Franck–Condon overlap, while lying in the same spectral range as the congested triplet band. For this reason, the photodetachment signal due to  ${}^1\text{HCCHO}$  is probably buried underneath the  $X^3A''$  band in Figure 3b. Often, the angular distributions corresponding to different photodetachment transitions can be used to identify the ground and excited states, but in the present study, the broad congested band from the triplet overwhelms any possible intensity from the singlet.

**4.2. Ketenyldiene Anion: Formation Mechanism.** The photoelectron image and spectrum of the  $m/z = 40$  anion presented in Figure 6 are in excellent agreement with previous results for  $\text{CCO}^{*-}$ ,<sup>15,16,27,28</sup> as discussed in section 3.3, leaving no doubt about the identity of the observed species. However, the formation of this anion in our ion source is both novel and interesting, because it must involve at least a two-step process that removes a net  $\text{H}_4^{*+}$  from  $\text{H}_3\text{CCHO}$ .

In Figure 10, we suggest a mechanism that assumes an initial  $\text{H}_2^{*+}$  abstraction to form either stable formylmethylene





Table 1. Thermochemical Quantities Either Used or Obtained in This Work (all values in kcal/mol)

no.	property	value	source
I	$\Delta_f H_{298}(\text{H})$	$52.103 \pm 0.001$	ref 48
II	$\Delta_f H_{298}(\text{H}_3\text{CCHO})$	$-40.80 \pm 0.35$	ref 49
III	$\Delta_f H_{298}(\text{H}_2\text{CCO})$	$-11.4 \pm 0.4$	ref 16
IV	$\Delta_f H_{298}(\text{H}_2\text{CCHO}^{\bullet})$	$1.4 \pm 2.2$	this work: eq 8, I, II, XVII
V	$\Delta_f H_{298}(\text{HCCO}^{\bullet})$	$42.4 \pm 2.1$	ref 16
VI	$\Delta_f H_{298}(\text{H}^+)$	$365.696 \pm 0.001$	refs 50 and 51
VII	$\Delta_f H_{298}(\text{H}_2\text{CCHO}^-)$	$-40.6 \pm 2.2$	this work: eq 9, II, VI, XV
VIII	$\Delta_f H_{298}(\text{CCO})$	$90.2 \pm 4.2^a$	this work: eq 8, I, V, XIX
IX	$\Delta_f H_{298}(\text{CCO})$	$68.499^b$	ref 46
X	$\Delta_f H_{298}(\text{CCO}^{\bullet-})$	$36.9 \pm 4.2$	this work: VII, XIII or eq 9, V, VI, XVI
XI	$\text{EA}(\text{H}_2\text{CCHO}^{\bullet})$	$42.0 \pm 0.2$	this work: experiment (Figure 5)
XII	$\text{EA}(\text{HCCHO})$	$43.1 \pm 0.5$	this work: experiment (Figure 3)
XIII	$\text{EA}(\text{CCO})$	$53.3 \pm 0.2$	this work: experiment (Figure 6)
XIV	$\text{IP}(\text{H})$	313.6	refs 46,50,51
XV	$\Delta_{\text{acid}} H_{298}(\text{H}_3\text{CCHO})$	$365.9 \pm 2.2$	ref 52
XVI	$\Delta_{\text{acid}} H_{298}(\text{HCCO}^{\bullet})$	$360.2 \pm 3.6$	ref 53
XVII	$\text{BDE}(\text{H}-\text{CH}_2\text{CHO})$	$94.3 \pm 2.2$	this work: eq 7, XI, XIV, XV
XVIII	$\text{BDE}(\text{H}_2\text{CC}(\text{O})-\text{H})$	$39.3 \pm 2.2$	this work: eq 8, I, III, IV
XIX	$\text{BDE}(\text{H}-\text{CCO}^{\bullet})$	$99.9 \pm 3.6$	this work eq 7, XIII, XIV, XVI

<sup>a</sup> Recommended value. <sup>b</sup> Presently reported on NIST Web site<sup>46</sup> (not recommended).

**4.3. Thermochemistry.** The electron affinities determined in this study can be used to calculate thermodynamic properties of the corresponding anions and radicals. Of primary interest are heats of formation ( $\Delta_f H_{298}$ ) and bond dissociation energies (denoted here as BDE, but also commonly referred to as  $DH_{298}$ ).

The R–H BDEs are calculated using the acidity/electron affinity cycle:<sup>44,45</sup>

$$\text{BDE}(\text{R}-\text{H}) = \Delta_{\text{acid}} H_{298}(\text{RH}) + \text{EA}(\text{R}) - \text{IP}(\text{H}) + [\text{thermal correction}] \quad (7)$$

where  $\text{IP}(\text{H})$  is the ionization potential of the hydrogen atom. The [thermal correction] term arises from integrated (0 to 298 K) differential heat capacities ( $\Delta C_p$ ) of the reactants and products. This term is small, typically about 0.3 kcal/mol. It is absorbed by other, larger uncertainties involved in the calculations and, therefore, disregarded from this point on. The thermochemical parameters used in our calculations and the results are summarized in Table 1. The source column either gives references for the previously known values or specifies how the new values were determined. Although multiple paths to a given quantity are possible within the self-consistent framework of thermodynamics, only a selected one or two are identified in each case.

For example, from the experimentally determined  $\text{EA}(\text{H}_2\text{CCHO}) = 1.82 \pm 0.01 \text{ eV} = 42.0 \pm 0.2 \text{ kcal/mol}$  (line XI in Table 1), we calculate, using eq 7, the C–H bond dissociation energy on the methyl group of acetaldehyde,  $\text{BDE}(\text{H}-\text{CH}_2\text{CHO}) = 94.3 \pm 2.2 \text{ kcal/mol}$  (line XVII). From the same calculation using the more precise SEVI value for the electron affinity ( $1.8250 \pm 0.0012 \text{ eV}$ ),<sup>12</sup> we obtain a  $\text{BDE} = 94.4 \pm 2.2 \text{ kcal/mol}$ , which is indistinguishable from our value. This comparison is, nonetheless, quite instructive, as it serves

to emphasize that the main contribution to the uncertainty comes from the measured acidity of acetaldehyde,  $\Delta_{\text{acid}} H_{298}(\text{H}_3\text{CCHO})$  (line XV in Table 1), and not the spectroscopic determination of electron affinity of the corresponding radical.

Bond dissociation energies and gas-phase acidities are related to the corresponding heats of formation:

$$\Delta_f H_{298}(\text{R}) = \text{BDE}(\text{R}-\text{H}) + \Delta_f H_{298}(\text{RH}) - \Delta_f H_{298}(\text{H}) \quad (8)$$

$$\Delta_f H_{298}(\text{R}^-) = \Delta_{\text{acid}} H_{298}(\text{RH}) + \Delta_f H_{298}(\text{RH}) - \Delta_f H_{298}(\text{H}^+) \quad (9)$$

Substituting the above result,  $\text{BDE}(\text{H}-\text{CH}_2\text{CHO}) = 94.3 \pm 2.2 \text{ kcal/mol}$  in eq 8, we obtain the formation enthalpy of the vinyoxy radical,  $\Delta_f H_{298}(\text{H}_2\text{CCHO}^{\bullet}) = 1.4 \pm 2.2 \text{ kcal/mol}$  (line IV).

The first C–H bond dissociation energy on the methyl group of acetaldehyde (94.3 kcal/mol, as determined above) is slightly smaller than many typical C–H BDEs. For comparison, in propane, the  $\text{H}-\text{CH}_2\text{CH}_2\text{CH}_3$  BDE is calculated to be  $100.4 \pm 3.4 \text{ kcal/mol}$ .<sup>44</sup> The small difference can be partially attributed to resonance stabilization of the unpaired electron in the vinyoxy radical resulting from acetaldehyde dissociation.

Vinyoxy radical has a planar structure, with the unpaired electron on the carbon radical center stabilized by resonance with the  $\pi$  electrons in the carbonyl bond. This radical can be regarded as an allyl radical ( $\text{H}_2\text{CCHCH}_2^{\bullet}$ ) with one of the methylene groups replaced by an oxygen atom. Allyl radical is formed by methyl C–H cleavage in propene ( $\text{CH}_3\text{CHCH}_2$ ) and the corresponding  $\text{BDE}(\text{H}-\text{CH}_2\text{CHCH}_2) = 88.8 \pm 0.4 \text{ kcal/mol}$ <sup>44</sup> is distinctly lower than the  $\text{BDE}(\text{H}-\text{CH}_2\text{CHO}) = 94.3 \pm 2.2 \text{ kcal/mol}$  obtained above. Allyl radical has two equivalent

resonance structures, with the radical site located on either of the terminal methylene groups. The double-resonance stabilization is reflected in the low BDE of propene. In vinoxy radical, on the other hand, the resonance structures are not equivalent: the configuration with a  $\pi$  bond on the more electronegative oxygen atom is dominant, while the structure with a  $\pi$  bond connecting the carbon atoms has a smaller contribution. As a result of the decreased resonance stabilization of the unpaired electron, acetaldehyde has a larger BDE, compared to propene.

In contrast,  $\text{BDE}(\text{H}_2\text{CC}(\text{O})-\text{H})$ , i.e., the C–H BDE of  $\text{H}_2\text{CCHO}^\bullet$  on the central carbon, to give  $\text{H}_2\text{CCO}$ , is determined to be only  $39.3 \pm 2.2$  kcal/mol (line XVIII in Table 1). This is less than half the energy of a C–H bond on the methylene and reflects the stability of ketene, in which the two unpaired electrons couple to form a CC  $\pi$  bond.

The thermochemistry of ketylenidene is obtained from the EA of CCO. Using our experimental  $\text{EA}(\text{CCO})$ , eq 7, and the thermochemical values in Table 1, we calculate  $\text{BDE}(\text{H}-\text{CCO}^\bullet) = 99.9 \pm 3.6$  kcal/mol (line XIX). The bond energy calculated using the SEVI value<sup>15</sup> for  $\text{EA}(\text{CCO})$  is  $100.1 \pm 3.6$  kcal/mol, which is, again, indistinguishable from our value (within the uncertainly limits). We also obtained  $\Delta_f H_{298}(\text{CCO}) = 90.2 \pm 4.2$  kcal/mol (line VIII). This result is in agreement with the previously reported value  $\Delta_f H_{298}(\text{CCO}) = 92.0 \pm 4.6$  kcal/mol,<sup>27</sup> although the agreement could be expected due to the use of similar thermochemical cycles. However, both of these values differ significantly from the value presently reported in the NIST Chemistry WebBook database,  $\Delta_f H_{298}(\text{CCO}) = 68.499$  kcal/mol (line IX).<sup>46</sup>

The correct value  $\Delta_f H_{298}(\text{CCO})$  is important both in itself and as a parameter used in calculating the thermodynamic properties of other species. In order to examine the above discrepancy, we used B3LYP/6-31+G(d) to estimate  $\text{BDE}(\text{H}-\text{CCO})$  and  $\text{BDE}(\text{C}-\text{CO})$  and compared the results with the corresponding BDE values obtained from eq 9 using  $\Delta_f H_{298}(\text{CCO}) = 90.2$  kcal/mol (this work) and 68.499 kcal/mol (NIST Chemistry WebBook<sup>46</sup>).

Substituting  $\Delta_f H_{298}(\text{CCO}) = 90.2$  kcal/mol in eq 9, we obtain  $\text{BDE}(\text{H}-\text{CCO}) = 99.9$  kcal/mol (Table 1, line XIX), in excellent agreement with the DFT prediction of 98 kcal/mol. Using eq 8 with  $\Delta_f H_{298}(\text{CCO}) = 68.499$  kcal/mol,<sup>46</sup> on the other hand, gives a much lower  $\text{BDE}(\text{H}-\text{CCO})$  value of 78 kcal/mol. Theory also predicts  $\text{BDE}(\text{C}-\text{CO}) = 60$  kcal/mol, in good agreement with the  $\text{BDE}(\text{C}-\text{CO})$  of 54.7 kcal/mol, obtained using  $\Delta_f H_{298}(\text{CCO}) = 90.2 \pm 4.2$  kcal/mol (this work) and the standard heats of formation of C and CO, 171.30 and  $-26.41$  kcal/mol,<sup>47</sup> respectively. The same calculation using  $\Delta_f H_{298}(\text{CCO}) = 68.499$  kcal/mol predicts a C–CO bond energy of 76.4 kcal/mol, which differs significantly from the DFT prediction. While DFT BDEs are not indisputable, the calculations support the findings based on our experimental measurements. Therefore, we recommend  $\Delta_f H_{298}(\text{CCO}) = 90.2 \pm 4.2$  kcal/mol.

## 5. CONCLUSIONS

We used photoelectron imaging spectroscopy to characterize the  $\text{HCCHO}^\bullet$ ,  $\text{H}_2\text{CCHO}^\bullet$ , and  $\text{CCO}^\bullet$  products of the reaction of  $\text{O}^\bullet$  with  $\text{H}_3\text{CCHO}$ . From photoelectron spectra of the formylmethylene anion, the electron affinity of  $\text{HCCHO}$  ( $1.87 \pm 0.02$  eV) and the detachment energies for two triplet bands are determined, but no unambiguous assignment for the

singlet state of  $\text{HCCHO}$  could be made. This is attributed to the singlet being an intermediate in the Wolff rearrangement, which results in formation of ketene; we therefore expect large geometry change (thus, poor Franck–Condon overlap) and fast rearrangement upon photodetachment to the singlet surface. The title reaction also provides a unique method for synthesizing  $\text{CCO}^\bullet$ , whose formation in our ion source is both novel and intriguing. A possible two-step mechanism for  $\text{CCO}^\bullet$  formation is suggested, involving an  $[\text{H}_2\text{CCO}^\bullet]^*$  intermediate. From the measured electron affinities of  $\text{HCCHO}$ ,  $\text{H}_2\text{CCHO}$ , and  $\text{CCO}$ , several new thermochemical properties have been determined, such as the C–H bond dissociation energies and heats of formation of some organic molecules and/or their anion. In particular, we determine the heat of formation of  $\text{CCO}$ ,  $\Delta_f H_{298}(\text{CCO}) = 90.2 \pm 4.2$  kcal/mol, and recommend revising the presently accepted value. Overall, the high reactivity of  $\text{O}^\bullet$  with organic molecules demonstrates the utility of this reagent in the formation of a variety of reactive intermediates via a single process.

## AUTHOR INFORMATION

### Corresponding Author

\*E-mail: sanov@u.arizona.edu.

### Present Addresses

<sup>†</sup>Department of Chemistry, University of Alabama, Tuscaloosa, AL.

## ACKNOWLEDGMENT

This work was supported by the U.S. National Science Foundation (grants CHE-071380 and CHE-1011895).

## REFERENCES

- (1) Harrison, A. G.; Jennings, K. R. *J. Chem. Soc., Faraday Trans. 1* **1976**, 72, 1601.
- (2) Lin, M. X.; Grabowski, J. J. *Int. J. Mass Spectrom.* **2004**, 237, 149.
- (3) Lee, J.; Grabowski, J. J. *Chem. Rev.* **1992**, 92, 1611.
- (4) Guo, Y.; Grabowski, J. J. *Abstr. Pap. Am. Chem. Soc.* **1990**, 199, 147.
- (5) Grabowski, J. J.; Melly, S. J. *Int. J. Mass Spectrom.* **1987**, 81, 147.
- (6) Kirmse, W. *Eur. J. Org. Chem.* **2002**, 2193.
- (7) Meier, H.; Zeller, K. P. *Angew. Chem., Int. Ed.* **1975**, 14, 32.
- (8) Kaplan, F.; Mitchell, M. L. *Tetrahedron Lett.* **1979**, 9, 759.
- (9) Wang, J.; Burdzinski, G.; Kubicki, J.; Platz, M. S. *J. Am. Chem. Soc.* **2009**, 130, 11195.
- (10) Burdzinski, G.; Wang, J.; Gustafson, T. L.; Platz, M. S. *J. Am. Chem. Soc.* **2008**, 130, 3746.
- (11) Litovitz, A. E.; Keresztes, I.; Carpenter, B. K. *J. Am. Chem. Soc.* **2008**, 130, 12085.
- (12) Yacovitch, T. I.; Garand, E.; Neumark, D. M. *J. Chem. Phys.* **2009**, 130, 244309.
- (13) Bowen, M. S.; Continetti, R. E. *J. Phys. Chem. A* **2004**, 108, 7827.
- (14) Alconcel, L. S.; Deyel, H. J.; Zengin, V.; Continetti, R. E. *J. Phys. Chem. A* **1999**, 103, 9190.
- (15) Garand, E.; Yacovitch, T. I.; Neumark, D. M. *J. Chem. Phys.* **2008**, 129, 074312.
- (16) Oakes, J. M.; Jones, M. E.; Bierbaum, V. M.; Ellison, G. B. *J. Phys. Chem.* **1983**, 87, 4810.
- (17) Velarde, L.; Habteyes, T.; Sanov, A. *J. Chem. Phys.* **2006**, 125, 114303.
- (18) Eppink, A.; Parker, D. H. *Rev. Sci. Instrum.* **1997**, 68, 3477.
- (19) Chandler, D. W.; Houston, P. L. *J. Chem. Phys.* **1987**, 87, 1445.
- (20) Dribinski, V.; Ossadtchi, A.; Mandelshtam, V. A.; Reisler, H. *Rev. Sci. Instrum.* **2002**, 73, 2634.

- (21) Cavanagh, S. J.; Gibson, S. T.; Gale, M. N.; Dedman, C. J.; Roberts, E. H.; Lewis, B. R. *Phys. Rev. A* **2007**, *76*, 052708.
- (22) Neumark, D. M.; Lykke, K. R.; Andersen, T.; Lineberger, W. C. *Phys. Rev. A* **1985**, *32*, 1890.
- (23) Cooper, J.; Zare, R. N. Photoelectron angular distributions. In *Atomic collision processes*; Geltman, S., Mahanthappa, K. T., Brittin, W. E., Eds.; Gordon and Breach, Science Publishers: New York, 1968; Vol. XI-C; p 317.
- (24) Cooper, J.; Zare, R. N. *J. Chem. Phys.* **1968**, *48*, 942.
- (25) Cooper, J.; Zare, R. N. *J. Chem. Phys.* **1968**, *49*, 4252.
- (26) Frisch, M. J. et al. *Gaussian 03, Revision C.02*; Gaussian, Inc.: Wallingford, CT, 2004.
- (27) Zengin, V.; Persson, B. J.; Strong, K. M.; Continetti, R. E. *J. Chem. Phys.* **1996**, *105*, 9740.
- (28) Choi, H.; Mordaunt, D. H.; Bise, R. T.; Taylor, T. R.; Neumark, D. M. *J. Chem. Phys.* **1998**, *108*, 4070.
- (29) Ellison, G. B.; Engelking, P. C.; Lineberger, W. C. *J. Phys. Chem.* **1982**, *86*, 4873.
- (30) Zimmerman, A. H.; Reed, K. J.; Brauman, J. I. *J. Am. Chem. Soc.* **1977**, *99*, 7203.
- (31) Mead, R. D.; Lykke, K. R.; Lineberger, W. C.; Marks, J.; Brauman, J. I. *J. Chem. Phys.* **1984**, *81*, 4883.
- (32) Jackson, R. L.; Hiberty, P. C.; Brauman, J. I. *J. Chem. Phys.* **1981**, *71*, 3705.
- (33) Surber, E.; Mabbs, R.; Sanov, A. *J. Phys. Chem. A* **2003**, *107*, 8215.
- (34) Tanaka, K.; Yoshimine, M. *J. Am. Chem. Soc.* **1980**, *102*, 7655.
- (35) Scott, A. P.; Nobes, R. H.; Schaefer, H. F., III; Radom, L. *J. Am. Chem. Soc.* **1994**, *116*, 10159.
- (36) Scott, A. P.; Platz, M. S.; Radom, L. *J. Am. Chem. Soc.* **2001**, *123*, 6069.
- (37) Holland, D. M. P.; Karlsson, L.; von Niessen, W. *J. Electron Spectrosc. Relat. Phenom.* **2001**, *113*, 221.
- (38) Toscano, J. P.; Platz, M. S. *J. Am. Chem. Soc.* **1995**, *117*, 4712.
- (39) Ervin, K. M.; Ho, J.; Lineberger, W. C. *J. Chem. Phys.* **1989**, *91*, 5974.
- (40) Goebbert, D. J.; Khuseynov, D.; Sanov, A. *J. Phys. Chem. A* **2010**, *114*, 2259.
- (41) Ichino, T.; Villano, S. M.; Gianola, A. J.; Goebbert, D. J.; Velarde, L.; Sanov, A.; Blanksby, S. J.; Zhou, X.; Hrovat, D. A.; Borden, W. T.; Lineberger, W. C. *Angew. Chem., Int. Ed.* **2009**, *48*, 8509.
- (42) Mozhayskiy, V.; Goebbert, D. J.; Velarde, L.; Sanov, A.; Krylov, A. I. *J. Phys. Chem. A* **2010**, *114*, 6935.
- (43) Ichino, T.; Villano, S. M.; Gianola, A. J.; Goebbert, D. J.; Velarde, L.; Sanov, A.; Blanksby, S. J.; Zhou, X.; Hrovat, D. A.; Borden, W. T.; Lineberger, W. C. *J. Phys. Chem. A* **2011**, *115*, 1634.
- (44) Blanksby, S. J.; Ellison, G. B. *Acc. Chem. Res.* **2003**, *36*, 255.
- (45) Goebbert, D. J.; Velarde, L.; Khuseynov, D.; Sanov, A. *J. Phys. Chem. Lett.* **2010**, *1*, 792.
- (46) Bartmess, J. E. Negative Ion Energetics Data. In *NIST Chemistry WebBook*; NIST Standard Reference Database Number 69; Linstrom, P. J., Mallard, W. G., Eds.; National Institute of Standards and Technology: Gaithersburg, MD, 2009; <http://webbook.nist.gov> (retrieved January 12, 2010).
- (47) *CRC Handbook of Chemistry and Physics*, 90th ed.; CRC Press: Boca Raton, FL, 2009–2010.
- (48) Cox, J. D.; Wagman, D. D.; Medvedev, V. A. *CODATA Key Values for Thermodynamics*; Hemisphere Publishing Corp.: New York, 1984.
- (49) Wiberg, K. B.; Crocker, L. S.; Morgan, K. M. *J. Am. Chem. Soc.* **1991**, *113*, 3447.
- (50) Goebbert, D. J.; Wenthold, P. G. *Int. J. Mass Spectrom.* **2006**, *257*, 1.
- (51) *NIST Chemistry WebBook*; NIST Standard Reference Database Number 69, June 2005 Release; Linstrom, P. J.; Mallard, W. G., Eds.; National Institute of Standards and Technology: Gaithersburg, MD, 2005.
- (52) Bartmess, J. E.; Scott, J. A.; McIver, R. T. *J. Am. Chem. Soc.* **1979**, *101*, 6047.
- (53) Van Doren, J. M.; Miller, T. M.; Stevens-Miller, A. E.; Viggiano, A. A.; Morris, A.; Paulson, J. F. *J. Am. Chem. Soc.* **1993**, *115*, 7407.